Interplay between faults and lava flows in construction of the upper oceanic crust: The East Pacific Rise crest 9°25'-9°58'N

J. Escartin, S. A Soule, D. J Fornari, M. A Tivey, H. Schouten, M. R Perfit

Geochemistry Geophysics Geosystems G3
AN ELECTRONIC JOURNAL OF THE EARTH SCIENCES
Published by AGU and the Geochemical Society

Article
Volume 8, Number 6
7 June 2007
Q06005, doi:10.1029/2006GC001399
ISSN: 1525-2027

Interplay between faults and lava flows in construction of the upper oceanic crust: The East Pacific Rise crest 9°25′–9°58′N

J. Escartín
Groupe de Géosciences Marines, IPGP, CNRS-INSU, 4 Place Jussieu, F-75005 Paris, France (escartin@ipgp.jussieu.fr)

S. A. Soule, D. J. Fornari, M. A. Tivey, and H. Schouten
Department of Geology and Geophysics, Woods Hole Oceanographic Institution, Woods Hole, Massachusetts 02543, USA

M. R. Perfit
Department of Geological Sciences, University of Florida, Gainesville, Florida 32611, USA

[1] The distribution of faults and fault characteristics along the East Pacific Rise (EPR) crest between 9°25′N and 9°58′N were studied using high-resolution side-scan sonar data and near-bottom bathymetric profiles. The resulting analysis shows important variations in the density of deformational features and tectonic strain estimates at young seafloor relative to older, sediment-covered seafloor of the same spreading age. We estimate that the expression of tectonic deformation and associated strain on "old" seafloor is ~5 times greater than that on "young" seafloor, owing to the frequent fault burial by recent lava flows. Thus the unseen, volcanically overprinted tectonic deformation may contribute from 30% to 100% of the ~300 m of subsidence required to fully build up the extrusive pile (Layer 2A). Many longer lava flows (greater than ~1 km) dam against inward facing fault scarps. This limits their length at distances of 1–2 km, which are coincident with where the extrusive layer acquires its full thickness. More than 2% of plate separation at the EPR is accommodated by brittle deformation, which consists mainly of inward facing faults (~70%). Faulting at the EPR crest occurs within the narrow, ~4 km wide upper crust that behaves as a brittle lid overlying the axial magma chamber. Deformation at greater distances off axis (up to 40 km) is accommodated by flexure of the lithosphere due to thermal subsidence, resulting in ~50% inward facing faults accommodating ~50% of the strain. On the basis of observed burial of faults by lava flows and damming of flows by fault scarps, we find that the development of Layer 2A is strongly controlled by low-relief growth faults that form at the ridge crest and its upper flanks. In turn, those faults have a profound impact on how lava flows are distributed along and across the ridge crest.

Components: 12,333 words, 9 figures, 2 tables.

Keywords: faulting; volcanism; mid-ocean ridge; East Pacific Rise; tectonic strain.

Index Terms: 1032 Geochemistry: Mid-oceanic ridge processes (3614, 8416); 8010 Structural Geology: Fractures and faults; 5480 Planetary Sciences: Solid Surface Planets: Volcanism (6063, 8148, 8450).

Received 26 June 2006; **Revised** 15 February 2007; **Accepted** 21 February 2007; **Published** 7 June 2007.

Escartín, J., S. A. Soule, D. J. Fornari, M. A. Tivey, H. Schouten, and M. R. Perfit (2007), Interplay between faults and lava flows in construction of the upper oceanic crust: The East Pacific Rise crest 9°25′–9°58′N, *Geochem. Geophys. Geosyst.*, *8*, Q06005, doi:10.1029/2006GC001399.

1. Introduction and Tectonic Setting

[2] The East Pacific Rise (EPR) between the Siqueiros and the Clipperton Fracture Zones, spreads at a full rate of ~110 km/Myr, and is one of the best studied portions of the world's mid-ocean ridge system [e.g., *Detrick et al.*, 1987; *Toomey et al.*, 1990, 1994; *Haymon et al.*, 1991, 1993; *Carbotte and MacDonald*, 1992; *Macdonald et al.*, 1992; *Kent et al.*, 1993; *Harding et al.*, 1993; *Christeson et al.*, 1994, 1996, 1997; *Perfit et al.*, 1994; *Lee and Solomon*, 1995; *Wright et al.*, 1995a, 1995b; *Collier and Singh*, 1997; *Fornari et al.*, 1998a, 1998b, 2004; *Cochran et al.*, 1999; *Schouten et al.*, 1999; *Engels et al.*, 2003; *Kurras et al.*, 2000; *Soule et al.*, 2005; *Bowles et al.*, 2006; *Ferrini et al.*, 2007] (Figure 1). The locus of spreading at the ridge crest is marked by a discontinuous, narrow axial summit trough (AST) of variable width (<50 m to ~400 m) and depth (<5 m to ~15 m) [*Fornari et al.*, 1998a, 2004; S. A. Soule et al., The axial summit trough of the East Pacific Rise 9°09′–59′N: New insights from DSL-120 side-scan and ABE sonar surveys, manuscript in preparation, 2007 (hereinafter referred to as Soule et al., manuscript in preparation, 2007)] (Figure 2). All known active hydrothermal vents and volcanic eruptions within the study area, including the 1991–92 and 2005–06 eruptions, occur along the AST [e.g., *Haymon et al.*, 1991, 1993; *Tolstoy et al.*, 2006; *Cowen et al.*, 2007], and are fed from an underlying axial magma chamber (AMC) ~1.2–2 km deep [*Detrick et al.*, 1987; *Harding et al.*, 1993; *Kent et al.*, 1993].

[3] The area along the ridge crest proximal to the AST is both the zone over which the extrusive layer (seismic Layer 2A) is formed, and where faults nucleate, grow, and interact with lava flows [e.g., *Macdonald et al.*, 1996; *Carbotte et al.*, 2003; *Cormier et al.*, 2003]. Lavas erupted at the AST flow across the ridge crest forming either short (<500 m), small-volume lobate flows or more voluminous and longer (>500–3000 m) flows fed by lava channels [*Fornari et al.*, 2004; *Soule et al.*, 2005; *Garry et al.*, 2006]. Off-axis volcanism, forming elongated pillow mounds probably associated with axis-parallel fissure eruptions, represents a volumetrically small portion of the extrusive layer [e.g., *Fornari et al.*, 1998a; *Perfit et al.*, 1994; *Perfit and Chadwick*, 1998; *White et al.*, 2000, 2002]. To explain the increase in Layer 2A thickness from ~100–200 m at the axis to its full thickness of ~300–500 m within 1–2 km from the axis [*Harding et al.*, 1993; *Vera and Diebold*, 1994; *Christeson et al.*, 1992, 1994, 1996; *Carbotte et al.*, 1997; *Bowles et al.*, 2006], numerical models require the emplacement of both short (~100 m) and long (>1000 m) lava flows [*Hooft et al.*, 1996], consistent with the field observations [e.g., *Fornari et al.*, 2004; *Soule et al.*, 2005; Soule et al., manuscript in preparation, 2007].

[4] Plate separation at fast spreading mid-ocean ridges (MORs) is primarily accommodated by magmatic accretion with faulting accounting for ~4% to 10% of the extension [e.g., *Cowie et al.*, 1993; *Bohnenstiehl and Carbotte*, 2001]. Faults form within 1–4 km of the EPR axis [e.g., *Searle*, 1984; *Wright et al.*, 1995a, 1995b; *Fornari et al.*, 1998a] and grow as the lithosphere is rafted off-axis [e.g., *Lee and Solomon*, 1995; *Alexander and Macdonald*, 1996; *Macdonald et al.*, 1996; *Crowder and Macdonald*, 2000]. Estimates of the active plate boundary vary from <10 km [*Edwards et al.*, 1991] to ~40 km off axis [*Lee and Solomon*, 1995; *Alexander and Macdonald*, 1996; *Crowder and Macdonald*, 2000]. We expect that the interaction between volcanism and tectonism, which has been documented off-axis where lava flows drape over preexisting outward facing faults [*Macdonald et al.*, 1996; *Carbotte et al.*, 1997], is greatest in the near-AST zone, where most eruptions occur. Faults at distances <4 km from the AST are typically short and display small throws (<10 m), and cannot be properly characterized with sea-surface multibeam or sonar systems typically used in fault studies of the oceanic crust [e.g., *Searle and Laughton*, 1977; *Searle*, 1984; *Edwards et al.*, 1991; *Macdonald et al.*, 1992; *Cowie et al.*, 1993, 1994; *Bohnenstiehl and Carbotte*, 2001]. The study of these small-scale features requires instead near-bottom high frequency sonar systems [e.g., *Deschamps et al.*, 2007] such as those used in this study, including: scanning altimetry (675 kHz) systems that provide <~0.5 m vertical resolution, and 120 kHz side-scan sonar that provides ~2 m pixel resolution backscatter imagery [*Scheirer et al.*, 2000; *Chadwick et al.*, 2001; *Carbotte et al.*, 2003; *Cormier et al.*, 2003; *Hey et al.*, 2004; *Fornari et al.*, 2004; *Soule et al.*, 2005; *Ferrini et al.*, 2007; Soule et al., manuscript in preparation, 2007].

[5] We present an analysis of high-resolution, near-bottom 120 kHz side-scan sonar data to investigate

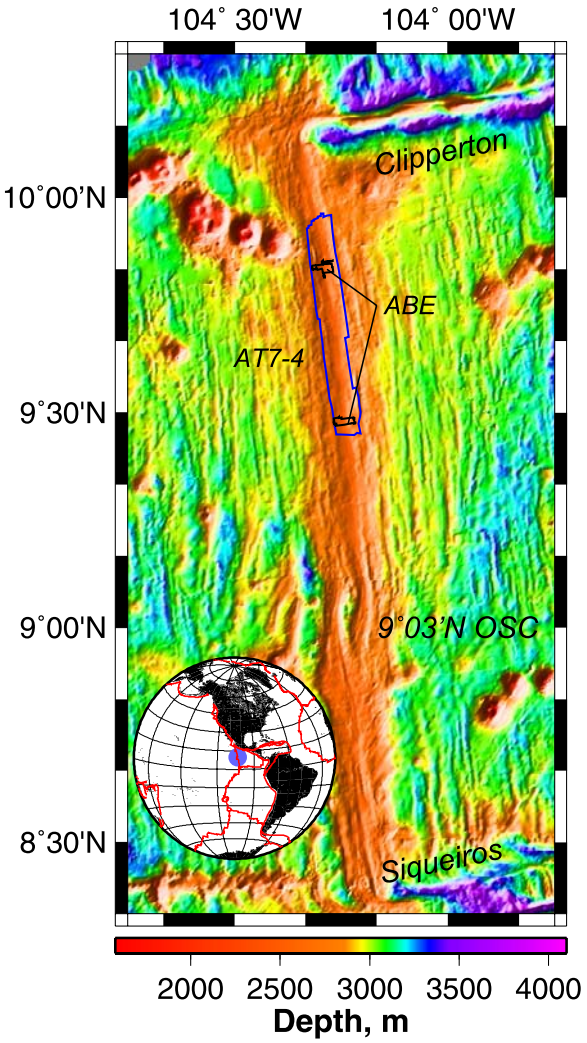

Figure 1. Shaded shipboard multibeam bathymetry of the East Pacific Rise between the Siqueiros and the Clipperton Fracture Zones [*Macdonald et al.*, 1992], showing the ridge axis and the off-axis seamounts. Outline of AT7-4 DSL-120a side-scan sonar survey (blue line) and near-bottom ABE altimeter surveys (ABE, black lines) shown. Inset shows location of the study area. OSC, overlapping spreading center.

fault distribution and density along a ~6 km wide zone on either side of the EPR axis between 9°25′N and 9°58′N (Figures 1 and 2). The sonar data allow us to differentiate between younger seafloor, recently repaved by volcanism, and older, sediment covered seafloor. These data clearly indicate that faults both limit the off-axis extent of flows, and are buried by lava flows, depending on the scarp height and the lava flow thickness and volume. By comparing fault characteristics both as a function of distance from the axis, and whether they form on "old" or "young" seafloor defined using the sonar data, we estimate the amount of tectonic strain that may be buried by volcanism in the immediate vicinity of the axis, and the distances at which faulting controls the off-axis extent of volcanic accretion. These data allow us to propose a model in which small-scale faulting plays an important role in the formation and growth of the extrusive volcanic layer at fast spreading MORs.

2. Data Processing and Interpretation

[6] Data sets used in this study include (1) an extensive DSL-120A high-resolution 120 kHz side-scan sonar survey covering ~95 km of the crest and upper flanks of the EPR and extending out to ~6 km off-axis [*Fornari et al.*, 2004; Soule et al., manuscript in preparation, 2007] (Figures 1 and 2); (2) two near-bottom 675 kHz scanning altimetric sonar surveys at 9°28′N and 9°50′N collected by the ABE autonomous underwater vehicle [e.g., *Yoerger et al.*, 1998; *Schouten et al.*, 2002; *Fornari et al.*, 2004] (Figure 1); and (3) high-resolution, near-bottom bathymetric profiles from Alvin dives and deep-tow digital camera (TowCam) collected during two cruises in 2001 and 2004 (AT7-4 and AT11-7, Figure 2) [*Fornari*, 2003; *Ferrini et al.*, 2007]. Data used in our study are also available online within a Geographic Information System (GIS) using ARC IMS (http://ortelius.whoi.edu/website/EPR_9N/viewer.htm).

[7] We mapped faults and fissures using the side-scan sonar data, and measured fault scarp heights wherever high-resolution ABE or TowCam bathymetry data were available. We determined the relative age of the seafloor ("young" or "old") on the basis of its acoustic character and visual confirmation from Alvin and TowCam imagery. We also mapped volcanic features, and combined them with results from more detailed studies of lava flows and channels by *Soule et al.* [2005] and Soule et al. (manuscript in preparation, 2007). The maps in Figure 2 provide a comprehensive view of the main geologic features of the EPR ridge crest and its upper flanks, and document the interaction of tectonic and volcanic processes during the last ~80–100 ka.

2.1. Side-Scan Sonar and Near-Bottom High-Resolution Bathymetry Data

[8] Side-scan sonar data were acquired during two cruises (2000 AHA-Nemo2 and 2001 AT7-4 cruises [*Fornari et al.*, 2004]) and have a ~2 m

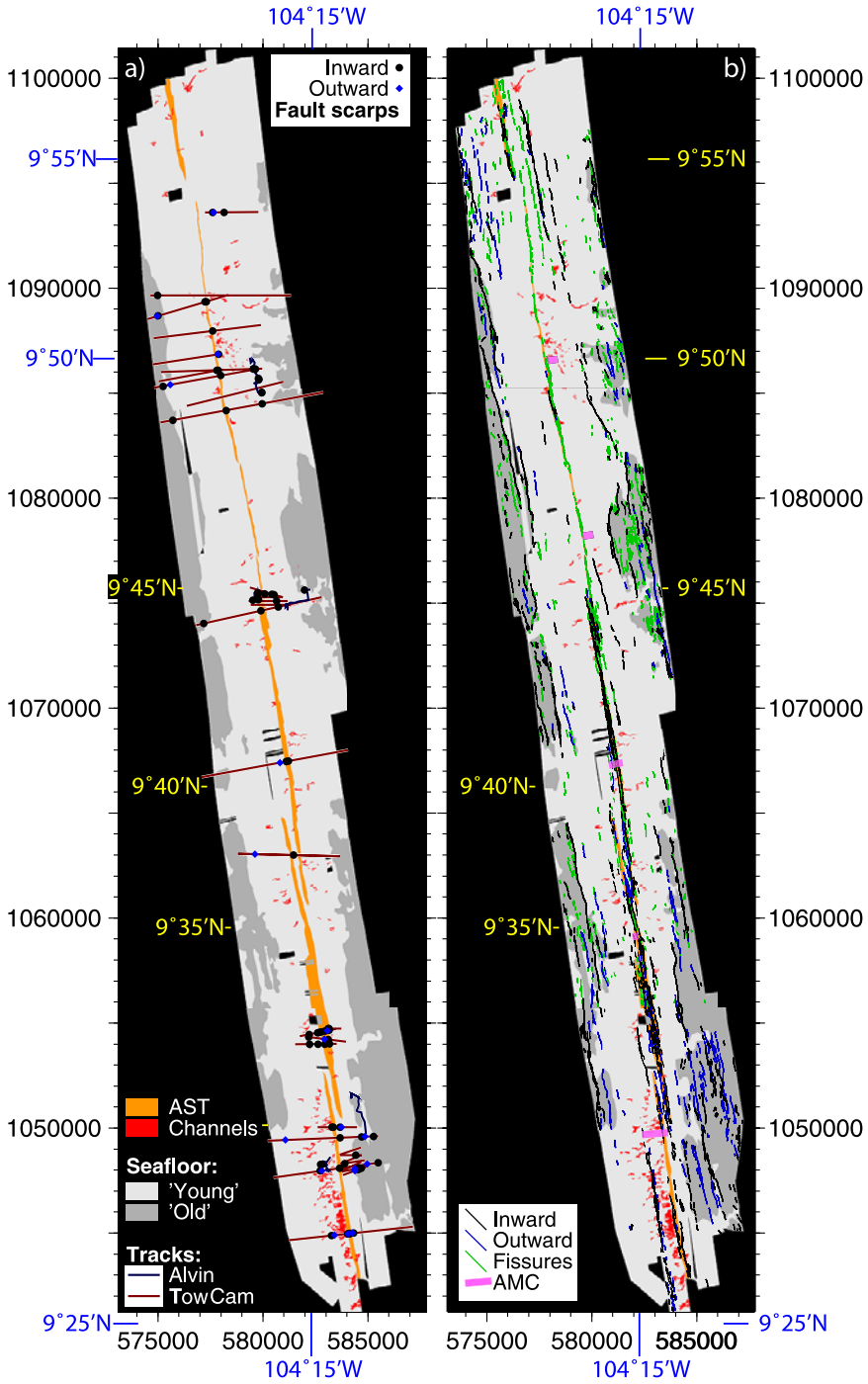

Figure 2. (a) Interpreted seafloor acoustic character and volcanic features, and location of TowCam traverses and Alvin tracks. The seafloor shows areas of high and low acoustic backscatter that correspond to unsedimented ("young" seafloor) and sedimented ("old" seafloor; see text). The axial summit trough (AST, orange) and lava channels (red, from *Soule et al.* [2005]) are also indicated. Fault scarp height measurements (circles) are limited and obtained from ABE bathymetry or high-resolution, near-bottom bathymetry data acquired along the TowCam or Alvin tracks. (b) Inward and outward facing faults and fissures interpreted from the high-resolution DSL120 side-scan sonar data. The across-axis extent of the AMC from seismic profiles is also shown [*Harding et al.*, 1993].

spatial resolution [*Scheirer et al.*, 2000]. Tracks were oriented at ~350°, subparallel to the ridge axis, with a horizontal accuracy better than 20–30 m. Sonar data were corrected for across-track variations in acoustic backscatter due to the decrease in the insonification angle from the nadir outward, using the vehicle altitude at the nadir and assuming a flat bottom [e.g., *Stewart et al.*, 1994; *Scheirer et al.*, 2000]. Owing to location errors, sonar swaths were locally hand-shifted and stretched to match features across adjacent tracks in the final mosaic.

[9] Near-bottom scanning altimetric sonar data at two sites along the EPR were acquired during ABE surveys (cruises AT7-4 and AT7-12 [*Fornari et al.*, 2004]). Gridded data, after navigation and vehicle attitude corrections, have spatial resolution of ~5 m horizontally and 1 m vertically. Additional high-resolution (~0.2 m vertical) bathymetry profiles throughout the study area were obtained during cruise AT11-7 using a 100 kHz altimeter and vehicle depth data along Alvin and TowCam tracks [*Fornari*, 2003] (Figure 2a). Alvin navigation was based on a combination of transponder fixes and Doppler velocity log (DVL) navigation [*Fornari et al.*, 1998a, 2004; *Singh et al.*, 2000; *Kinsey and Whitcomb*, 2002, 2004; *Ferrini et al.*, 2007]. On AT11-7 the TowCam was navigated using the ship's GPS position and a lay-back calculation, later adjusted by matching topographic features along the bathymetric profiles with structures (i.e., volcanic mounds, scarps, AST walls) visible in the sonar or the ABE bathymetry. On AT7-4, camera surveys were navigated using a network of bottom-moored acoustic transponders.

2.2. Geographic Correlation Among Data Sets

[10] The AT7-4 side-scan sonar data set provides the most complete coverage of the study area, and is the basis for our fault interpretation. The sonar survey was thus chosen as the reference data set to relocate the near-bottom bathymetric profiles. Differences in navigation techniques for these data sets result in offsets of up to 50–100 m between the ABE microbathymetry and the side-scan sonar (Soule et al., manuscript in preparation, 2007).

2.3. Acoustic Character and Relative Seafloor Age

[11] The acoustic backscatter intensity in the study area shows a bimodal distribution, with acoustically reflective (bright) areas near the AST, and less reflective terrain (dark) away from it (Figures 2 and 3). Seafloor reflectivity depends primarily on slope, sediment cover [e.g., *Mitchell*, 1993], and to a lesser degree on lava texture (roughness). In the study area, seafloor slopes across side-scan track lines are gentle (<5°); hence the sonar mosaics can be easily interpreted to differentiate between sedimented and unsedimented seafloor, a qualitative proxy for seafloor age. In most cases boundaries between acoustically bright seafloor (unsedimented and therefore "young") and less reflective ("old") seafloor is sharp (Figure 3). These boundaries correspond to young lava flows ponded at the base of fault scarps (Figures 3a and 3b), or edges of young lava flows emplaced over "old" seafloor (Figures 3c and 3d). The "young" seafloor shows either a scalloped texture corresponding to curved fronts of small lava flows, or is blanketed by larger lava flows fed by collapsed lava tubes or channels that may extend out to several kilometers off-axis [*Fornari et al.*, 2004; *Soule et al.*, 2005; Soule et al., manuscript in preparation, 2007].

[12] Repaving of the EPR crestal plateau by recent lava flows (Figure 3) results in seafloor ages younger than the spreading age (distance from axis/spreading rate). This process is common at the EPR and is confirmed by U-series disequilibria dating of basalts in the study area [*Goldstein et al.*, 1993; *Sims et al.*, 2003; *Sohn and Sims*, 2005]. In those studies, most samples located within ~3.5 km from the axis show near-zero ages, and lie within "young" seafloor. A few additional near-zero ages samples correspond to pillow mounds that appear to have erupted off-axis [e.g., *Perfit et al.*, 1994]. Samples that have radiometric model ages in agreement with their spreading ages are located within or in the immediate vicinity of "old" seafloor. On the basis of available U-series data and correlation with seafloor acoustic character we infer that the mapped "young" and "old" terrains in Figure 2 correspond to differences in

Figure 3. (a and c) Side-scan sonar images, (b and d) corresponding interpretation, and (e and f) corresponding high-resolution bathymetric profiles showing the boundary between "young," reflective unsedimented, and "old" sedimented seafloor. The "young"/"old" seafloor boundary is sharp throughout most of the study area (Figure 2) and corresponds primarily to ponding of lava flows against fault scarps (e.g., west side of axis in Figures 3a and 3b) and to lava flow emplacement over older seafloor (east side of axis in Figures 3c and 3d).

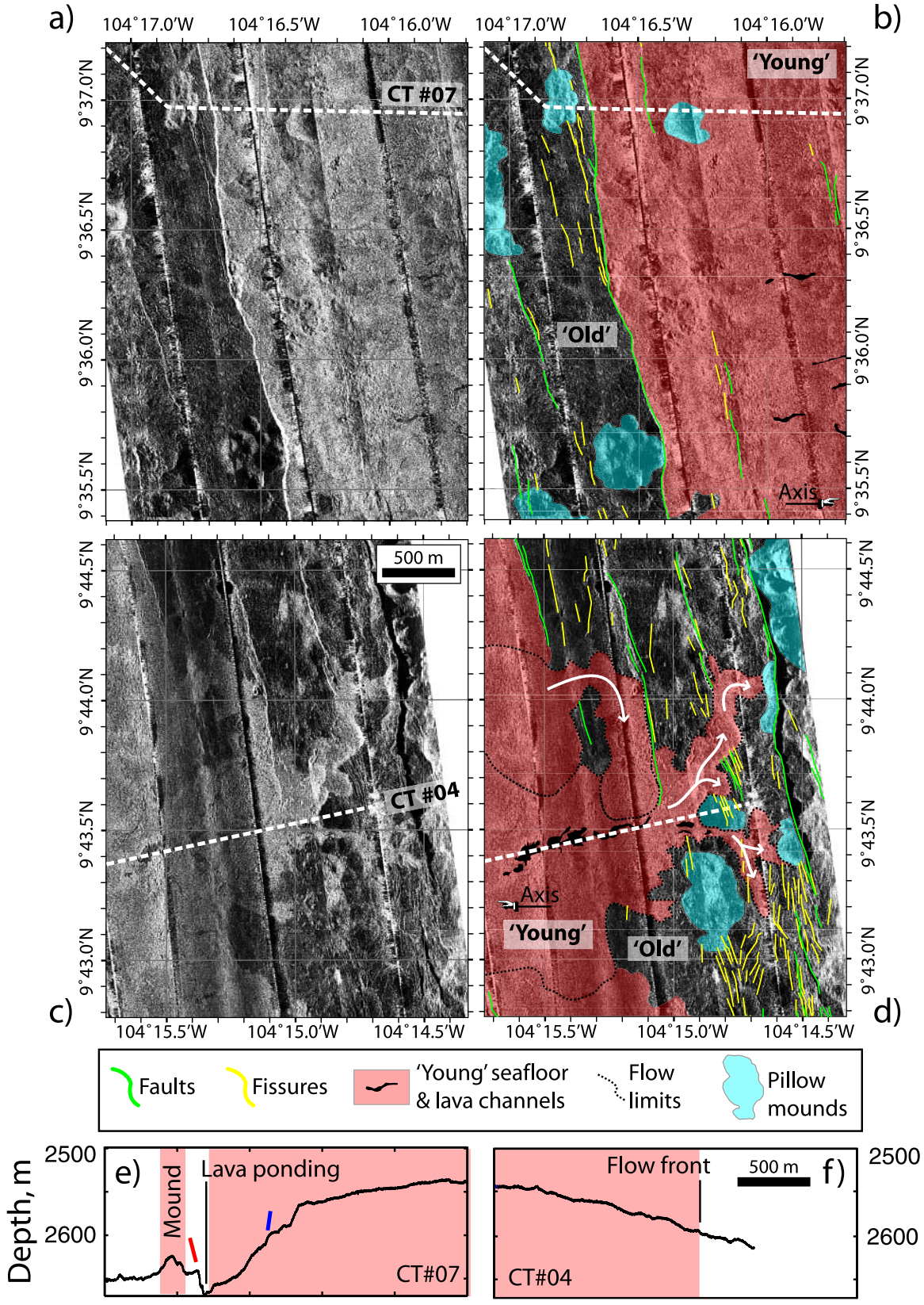
a)
b)
c)
d)
104°17.0'W
104°16.5'W
104°16.0'W
104°15.5'W
104°15.0'W
104°14.5'W
9°37.0'N
9°36.5'N
9°36.0'N
9°35.5'N
9°44.5'N
9°44.0'N
9°43.5'N
9°43.0'N
CT #07
CT #04
'Young'
'Old'
Axis
500 m
Faults
Fissures
'Young' seafloor & lava channels
Flow limits
Pillow mounds
Depth, m
2500
2600
e)
Mound
Lava ponding
CT#07
Flow front
500 m
f)
CT#04

Figure 3

seafloor age of the order of ~1–10 kyrs. Observed along-axis variations in the width and asymmetry of "young" seafloor allow us to quantify faulting, fissuring, and tectonic strain in crust of the same spreading age (i.e., at the same distance from the AST). This provides a window into the amount of tectonic deformation that is obscured by more recent volcanism, and can be used as a tool to understand the impact of faulting on lava emplacement at a fast spreading MOR axis.

2.4. Tectonic Features: Faults and Fissures

[13] We mapped fault and fissure traces in the side-scan data, and determined the fault dip direction relative to the axis (inward or outward facing) on the basis of the insonification geometry and backscatter character. Fault traces shown in Figure 2b correspond to the top of fault scarps, and the fissure traces to their centerline. We were not able to determine cumulative size-frequency distributions of fault parameters (spacing, displacement, length) or length-displacement relationships [e.g., *Dawers et al.*, 1993; *Carbotte and MacDonald*, 1994; *Cowie et al.*, 1994; *Deschamps et al.*, 2007] due to a lack of sufficient high-resolution bathymetric coverage, as they require a proper characterization of the fault system with denser data. Fault spacing measurements require long profiles across numerous faults [e.g., *Soliva et al.*, 2006], and are not feasible using the data currently available owing to the narrow width of the study area (~3 km off-axis on either side in average) compared with the typical fault spacing (~1 km). Accurate fault throw measurements are scarce in the data set, and do not provide a statistically significant number of observations.

[14] We analyze and interpret our results on fault and fissure trace densities (cumulative trace length per unit area, km/km^2) as a proxy for deformation intensity and tectonic strain. Variable insonification geometry of faults, in addition to their small size (<10 m in vertical throw in most cases), does not allow us to constrain fault scarp width, which could be used as a proxy for horizontal fault displacement [e.g., *Escartín et al.*, 1999]. As a result, tectonic strain cannot be directly measured from the side-scan sonar data.

[15] The depth of the AST varies along the axis (from >400 m to <50 m; Figure 2a). It is characterized by complex fissuring, faulting, and mass wasting along its walls and the terrain immediately flanking it [*Fornari et al.*, 1998a, 2004; Soule et al., manuscript in preparation, 2007]. Most of the AST-related tectonic features are complex and likely represent deformation induced by dike emplacement, axial eruptions, and subsequent drain back of lava into the AST [*Fornari et al.*, 1998a, 2004; Soule et al., manuscript in preparation, 2007]. The disappearance of linear deformational structures at distances >300 m to either side of the AST indicates that they are systematically buried by the most recent volcanic eruptions. For instance, this process is evident at 9°55′N where the AST has been completely filled by a recent eruption, and only discontinuous fissuring marks the axis (Figure 2). Fissure and fault parameter statistics (Table 1) are calculated for the study area, and for three subregions: the AST and nearby area, "young" seafloor, and "old" seafloor (Figure 2). For our calculations, the AST area is defined as crust <250 m from the AST center, thus encompassing seafloor with buried deformational structures associated with it [*Fornari et al.*, 1998a, 2004; Soule et al., manuscript in preparation, 2007].

3. Observations

3.1. Transition From "Young" to "Old" Crust

[16] The abrupt transitions from "young" to "old" seafloor are well defined throughout most of the study area (Figure 2). The most common transition corresponds to topographic barriers; mainly inward facing fault scarps and occasionally off-axis volcanic mounds that dam lava flows. Fault scarps define axis-parallel linear boundaries >10 km in length (Figures 2b, 3a, and 3c), and provide an important control on the width of "young" seafloor on either side of the EPR axis. While off-axis fault studies show that fault formation and distribution is mostly symmetric over long periods of time [e.g., *Carbotte and MacDonald*, 1994; *Bohnenstiehl and Carbotte*, 2001], both nucleation of and strain localization along individual faults may result in asymmetric fault distribution over short time periods. Another common "young"/"old" transition corresponds to the edges of recent flows that extend to distances of >2 km off-axis while flowing over "old" seafloor (see Figures 2b and Figures 3b and 3d). These flows had no interaction with structural barriers such as faults or overtopped them or were diverted parallel to them following gentle along-axis gradients (see Figures 3b and 3d). In these cases the transition between the "young" and "old" seafloor is thus controlled by the volume and eruption rate of the lava and the preexisting topography that they encounter [*Soule et al.*, 2005]. The longest lava flows often pond against larger

Table 1. Summary of Tectonic Parameters for "Recent" and "Old" Seafloor, the AST Zone, and the Whole Study Area[a]

	All[b]	"Young" Crust[b]	"Old" Crust[b]	AST
Fissures				
Length,[c] m	196 ± 132 (1318)	191 ± 120 (514)	200 ± 139 (804)	-
Density,[d] km/km^2	0.80	0.40	2.05	3.49
All faults				
Length,[c] m	392 ± 390 (936)	379 ± 329 (361)	402 ± 424 (575)	-
Density,[d] km/km^2	1.12	0.59	2.77	4.24
Inward facing faults				
Length,[c] m	392 ± 405 (632)	383 ± 352 (239)	398 ± 434 (393)	-
Height,[c] m	8.0 ± 10.9 (80)	6.0 ± 11.2 (50)	11.37 ± 9.65 (30)	4.1 ± 2.41 (53)
Density,[d] km/km^2	0.76	0.40	1.87	3.08
Outward facing faults				
Length,[c] m	393 ± 356 (304)	371 ± 280 (122)	408 ± 400 (182)	-
Height,[c] m	5.61 ± 4.2 (30)	4.7 ± 2.1 (20)	7.4 ± 6.5 (10)	3.2 ± 1.6 (16)
Density,[d] km/km^2	0.36	0.19	0.90	0.19
% Inward facing faults[e]				
Number of faults	68%	66%	68%	-
Fault length	68%	68%	68%	-
Strain	80%	71%	89%	
Strain[f]				
Total	0.7 ± 1.0%	0.5 ± 1.0%	2.1 ± 2.3%	-
Inward	0.6 ± 1.0%	0.4 ± 1.0%	1.6 ± 1.8%	-
Outward	0.1 ± 0.2%	<0.1 ± 0.1%	0.5 ± 0.7%	-

[a] Tectonic parameters included are fault and fissure length, fault scarp height, density, % of inward facing faults, and tectonic strain.
[b] The AST area (distances >250 m from the AST center) is excluded in the calculations so as to include tectonic features developed by tectonic extension, and eliminate those related to the AST formation.
[c] Average length or fault scarp height ± standard deviation. The number of observations (faults or fissures) is given in parentheses.
[d] Cumulative fault length (km) per surface (km^2).
[e] Percentage (%) of inward facing faults estimated from the fault number, the cumulative fault length, and the calculated strain along bathymetric transects.
[f] Strain estimates from cumulative fault height measured along 31 bathymetric transects obtained with the TowCam system. A 45° fault angle is assumed to infer horizontal fault displacement from cumulative vertical fault scarp height (see text and details given by *Escartín et al.* [1999] and *Bohnenstiehl and Carbotte* [2001].

fault scarps or graben that develop at the base of the crestal plateau and drape over outward facing faults [e.g., *Macdonald et al.*, 1996] (Figure 3). Small fault scarps (<10 m high) within "young" seafloor are likely to block the progress of the most recent, short and thin (1–2 m thick) lava flows. We suggest that large variations (<1 km to >5 km) in width and overall asymmetry of "young" seafloor in the study area (Figure 2) is controlled by the interplay between the frequency at which lava is transported across and down the ridge crest and flanks, versus the presence and development of fault scarps with sufficient height (>2 m) that may impede their progress.

3.2. Across-Axis Variations in Deformation Intensity and Fault Characteristics: "Young" Versus "Old" Seafloor

[17] We calculate fault and fissure characteristics in "young" and "old" volcanic provinces, and exploit the along-axis variation in width and asymmetry of "young" seafloor to examine differences in these tectonic indicators in crust of the same spreading age (Table 1; Figures 4 and Figures 5a and 5b). Faults within or near the AST are excluded from this analysis. The average fissure length (~200 m) is about half the average fault length (~390 m) with no significant differences between "young" and "old" seafloor. Inward and outward facing fault lengths are similar within each zone and faults are only slightly longer in "old" when compared with "young" seafloor (Table 1). In contrast, the average fault scarp height in "old" seafloor is significantly greater than that in "young" seafloor for both inward facing (~11 m versus ~6 m) and outward facing faults (~7 m versus ~5 m). Heights associated with the AST bounding scarps are on average ~4 m and ~3 m for inward and outward facing scarps, respectively. In all cases the standard deviation is large due to the low number of measurements and the scarp height variability (Table 1 and Figures 5a and 5b).

[18] Measured fissure and fault densities provide a quantitative estimate of the amount of deformation,

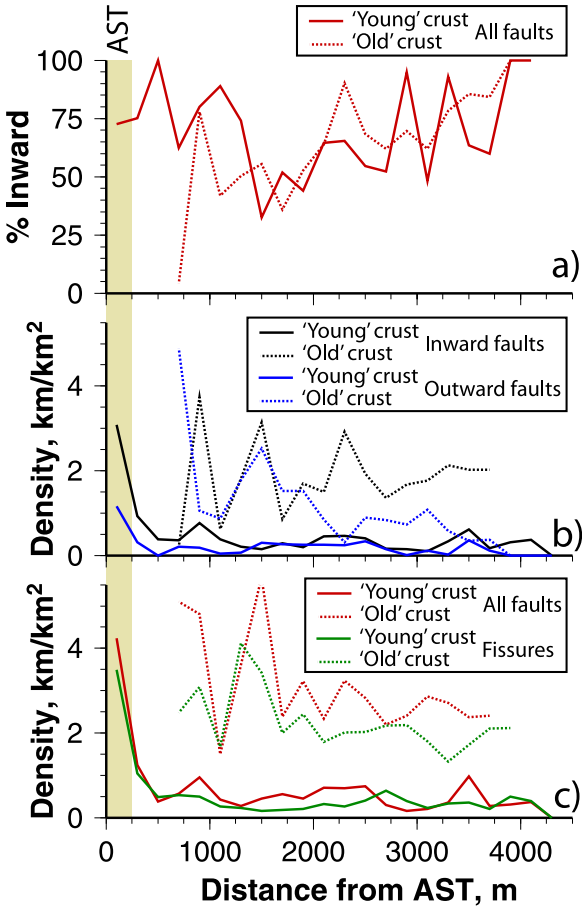

Figure 4. (a) Percent of inward facing faults, (b) density of inward and outward facing faults, and (c) density of faulting and fissuring as a function of distance from the AST center in 200-m-wide bins. Data from both the east and west flank are combined, as the overall paucity of tectonic features precludes detailed studies of smaller areas. The variable width of the "young" seafloor facilitates the comparison of deformation intensity between "old" and "young" seafloor at the same distance (spreading age) from the AST. Percent of inward facing faults is calculated from the cumulative length of inward and outward facing faults.

and show patterns consistent with those observed in the fault height data. Fissure and fault densities in the near–AST area are highest (3.5 and 4.2 km/km^2, respectively), whereas in "old" seafloor fissure and fault densities (2.05 and 2.77 km/km^2, respectively) are about five times higher than those in "young" seafloor (0.4 and 0.6 km/km^2, Table 1). We observe large fluctuations in the proportion of inward facing faults (Figure 4a), and fault and fissure densities (Figures 4b and 4c) with distance from the AST (i.e., spreading age), which are not reflected in the averages in Table 1. These fluctuations result from the small area of the across-axis bins and the large tectonic variability throughout the study area, and are not believed to reflect actual temporal variations.

[19] Approximately 70% of the faults in both "young" and "old" seafloor are inward facing, as determined both from the number of faults and the fault density measurements (Table 1). Outward facing fault density decreases from 1–2 km/km^2 near the AST to <1 km/km^2 further off-axis (Figure 4b). Inward facing faults, although dominant throughout the study area, show a minimum density at ~2 km from the AST center in "young" seafloor (~50%), and increase both toward the axis (excluding the AST and nearby seafloor) and off-axis (~75%). "Old" seafloor shows a progressive increase in the proportion of inward facing faults off-axis from <50% to >75% (Figure 4a). While Figure 5 shows that inward facing faults have larger throws on "old" seafloor

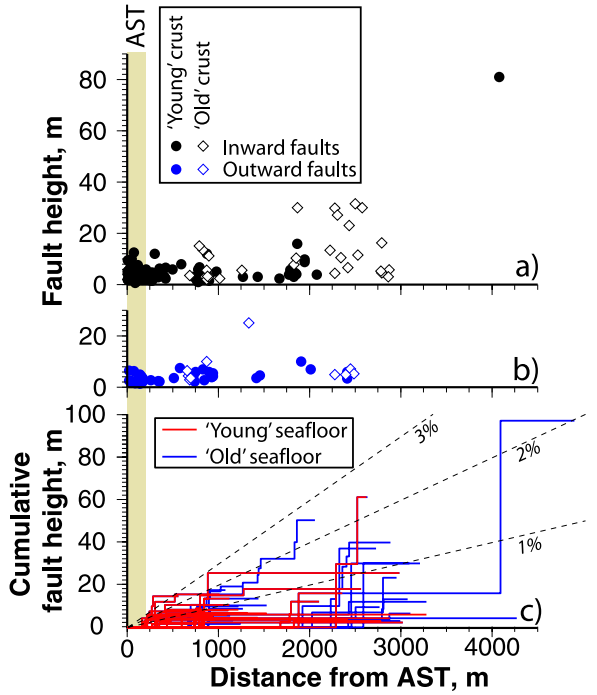

Figure 5. (a and b) Fault scarp height variations and (c) cumulative fault throw versus distance from the AST. Inward facing faults (Figure 5a) show a general increase of the maximum vertical fault height with distance from the AST. Outward facing faults are scarce and tend to have lower relief, and no clear trend away from the AST is observed. Heights of fault scarps on "old" terrain are significantly larger than those on "young" seafloor (see Table 1). The cumulative fault throw (Figure 5c) shows steeper lines for "old" seafloor (blue) when compared to "young" seafloor (red). Dashed lines correspond to homogeneous tectonic strain of 1%, 2%, and 3%, assuming a 45° fault dip.

than those on "young" seafloor (e.g., Table 1), the paucity of data does not reveal any spatial-temporal trend.

[20] We estimate tectonic strain from cumulative fault throw along 31 transects from near-bottom TowCam bathymetric profiles (Figures 2a and 5c). Distance is corrected for the angle between the profile and the spreading direction, and we infer cumulative horizontal strain from the cumulative fault height, assuming a 45° fault angle (see *Escartín et al.* [1999] and *Bohnenstiehl and Carbotte* [2001] for full details; Figure 5c). Strain estimates are four times higher on "old" seafloor (2.1 ± 2.3%) than on "young" seafloor (0.5 ± 1.0%), but the data show large variability owing to the scarce number of fault height data and transects, and their limited length (Figures 2a and 5). Inward facing faults accommodate ~80% of the measured strain in all cases, consistent with the 70% estimate both from the number and the density of faults (Table 1). The strain estimates also correlate well with the differences in fault density between "young" and "old" seafloor (0.6 versus 2.8 km/km^2, respectively, for all faults; Table 1). While the strain data are limited, they are coherent with tectonic parameters estimated from digitized fault and fissure traces, demonstrating that fault density is a good proxy for tectonic strain. This observation allows us to study areas with small fault scarps and very low tectonic strains.

3.3. Topography, Volcanic Emplacement, and Subsidence

[21] The EPR crestal volume shows along-axis variations both in the magnitude and polarity of the asymmetry [*Soule et al.*, 2005] that are interpreted to reflect differences in volcanic construction processes. Across-axis, high-resolution bathymetry (Figures 6 and 7,Table 2), combined with the extent of recently repaved, "young" seafloor, provide a much more detailed view of this asymmetry with time. Average differences in depth H of adjacent flanks between "young" seafloor and "old" and "young" seafloor (see a and b, respectively, in top profile of Figure 6 and Table 2) can be interpreted as resulting from fault-related subsidence, asymmetry in the emplacement of the extrusives, or a combination of both.

[22] Differences in the depth profiles of conjugate flanks based on near-bottom TowCam profiles within "young" seafloor vary between <1 m and >40 m on average, with maximum differences of 120 m. While 5 out of 9 profiles are effectively symmetrical (H < 5 m over distances >1–2 km, Table 2), with the most extreme asymmetry is observed at 9°51.4′N, with H > 42 m and corresponding to the maximum depth difference in the area. The largest H values are found in profiles with faults bounding well-developed off-axis (>1 km) graben (e.g., Profiles at 9°51.4′N and 9°29.6′N, Figure 6, Table 2), which dam recent lava flows. These also show the maximum absolute differences in depth, reaching >100 m. While we lack any subsurface data, bathymetric profiles suggest that preexisting graben have been in-filled partially or completely, resulting in flat areas of the crest away from the AST (see arrows in Figure 6). In the absence of graben, depth differences are smaller (<50 m), and do not seem to be associated with any visible faulting at the seafloor. The comparison of "young" and "old" seafloor at the same distance from the AST indicates that in most cases (5 out of 8) "old" seafloor is deeper than "young" seafloor. We observe no clear along-axis trend, nor correlation with the with of the AMC as reported by *Harding et al.* [1993] (Figures 2b and 6).

[23] Side-scan sonar and bathymetry data near 9°29′N (Figure 7), along with seafloor images along the profile at 9°29.6N (Figure 6 and Table 2) define an asymmetric emplacement of lava flows and their interaction with faults in detail. In this area, "old" seafloor east of the AST is dissected by two graben bound by inward and outward facing faults (Figure 7b). The difference is in the bathymetry between "young" seafloor on the west and "old" seafloor on the east flank, and its along-axis extension corresponds to a volume of ~70×10^6 m^3 per km of ridge axis (Figure 7c). The eastern transition between "young" and "old" seafloor is a complex juxtaposition of fronts of flows that have infilled the small graben ~500 m east of the AST (Figure 7d).

[24] Bathymetric profiles across the eastern graben (Figures 7b and 7d) show that the inward facing fault scarp height varies over a distance of <1 km, with a maximum height of ~25 m on (Profile A, Figures 7b and 7d). Scarp height is reduced to ~10 m by a flow (Profile C) that ponded within the graben and partially filled it. Flow fronts and mounds associated with a younger lava flow completely in-fill a portion of the graben, completely burying the fault scarp (Profile B). The bathymetric expression of the graben's outward facing fault is continuous, owing to draping by flows [e.g., *Macdonald et al.*, 1996]. This area shows a marked asymmetry in the occurrence of lava channels and collapsed tubes, which are concentrated in the area

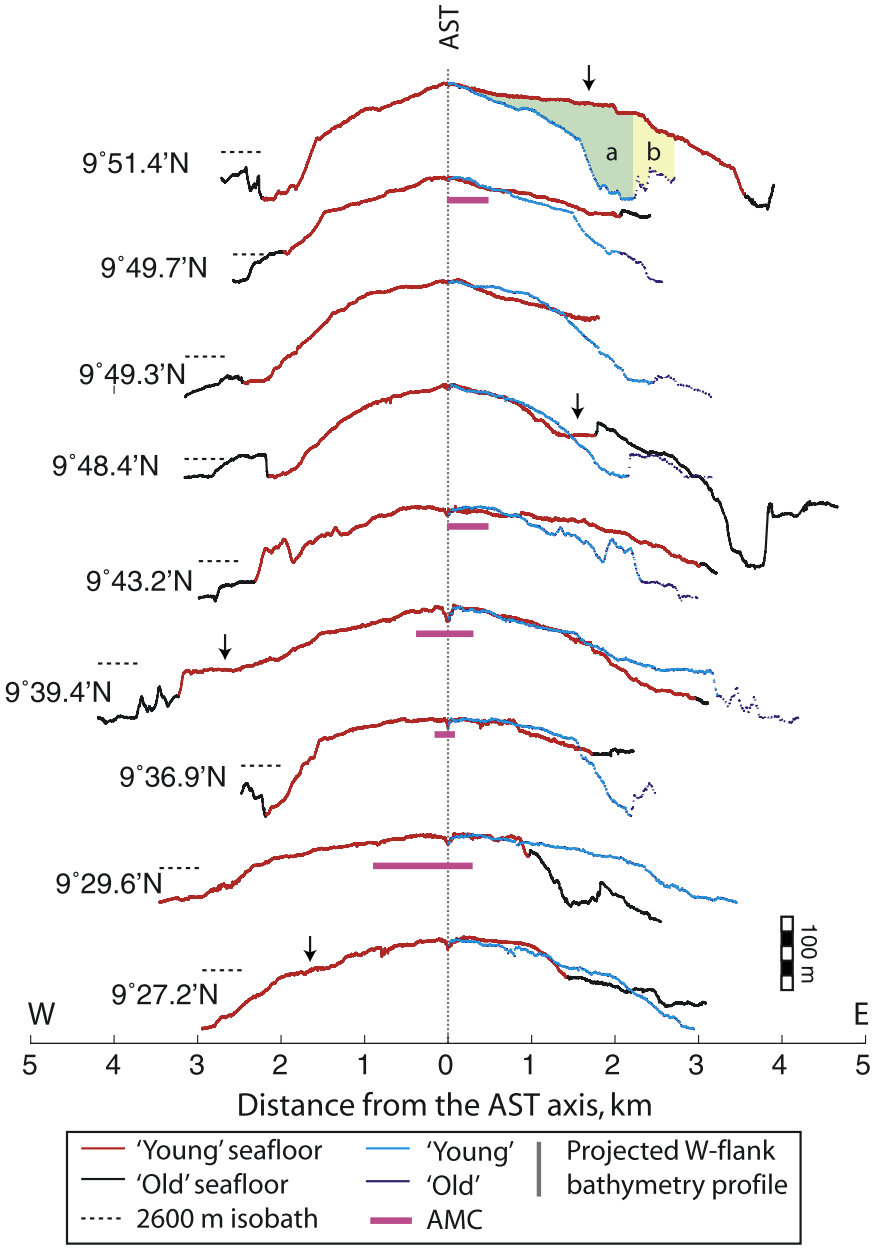

Figure 6. Stacked high-resolution bathymetric profiles across the EPR axis acquired with the TowCam system. "Young" seafloor is shown in red, and "old" seafloor is shown in black, as interpreted from the side-scan sonar mosaics (see Figure 2). The west-flank profile is projected on the east flank (blue) for comparison and to show the asymmetry. Dashed line corresponds to the 2600 m isobath, and latitudes correspond to that of each TowCam profile at the AST crossing. The shaded areas in the top profiles correspond to the difference in seafloor depth between adjacent flanks, for "young" seafloor (a) and for "young" versus "old" seafloor (b; see Table 2). Arrows mark flat or low-dipping areas that may correspond to infilled and buried graben by lava flows. The lateral extent of AMC at ~9°5′N, 9°45.4′N, 9°39.4′N, and 9°34.9′N from *Harding et al.* [1993] are plotted along the closest profile (see locations in Figure 2b).

west of the AST (see Figures 7a and 7b and *Soule et al.* [2005]). Only a small portion of the young eruptions sourced at the AST overflowed to the east, resulting in the narrow, ~500 m wide "young" seafloor east of the AST in the 9°28′N region. This asymmetry is controlled by the morphology of the AST [*Soule et al.*, 2005]. The western AST rim is ~2–3 m deeper on average than the eastern rim, with the total AST depth (rim to floor) varying from ~10 m to ~5 m over 1.4 km (Figure 7e). We

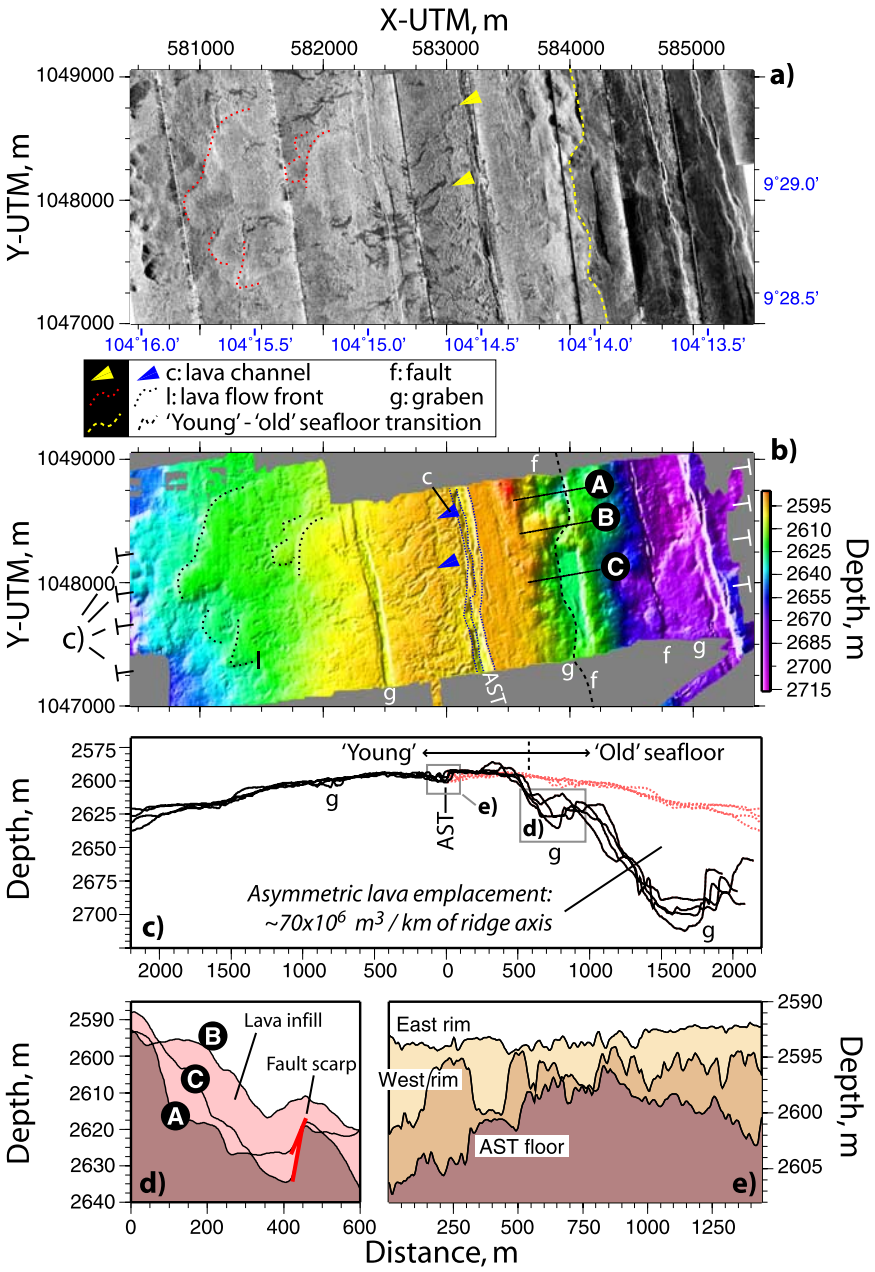

Figure 7. (a) Side-scan sonar mosaic and (b) ABE high-resolution bathymetry of the EPR axis at ~9°28′N (axes in UTM coordinates, meters). The "young"-to-"old" seafloor transition is indicated by a heavy dashed line, and selected flow fronts are indicated by a light dashed line. (c) Stacked across-axis profiles showing 75 m difference in depth between "old" and "young" seafloor at the same distance from the AST. Red line is bathymetric profile of the west flank projected onto the east flank for comparison. Locations of profiles shown in Figure 7b. (d) Detailed bathymetry profiles across the "old"-to-"young" seafloor transition east of the AST that coincides with lava flows partially infilling an off-axis graben. The outward facing fault is covered by the flows, and the inward facing fault shows variable vertical throws as it is covered in places by subsequent flows. Locations of profiles in Figures 7b and 7c. (e) Bathymetric profiles along the center of the AST, and along its east and west rims, shown by dotted lines in Figures 7b and 7c. The ~2 km long bathymetric profile along the west rim is 2–3 meters lower than that of the west rim. This AST morphology has controlled the preferential flow of lava toward the west over the last >1000 years, resulting in a marked asymmetry in the bathymetry of the crest and in a wider "young" seafloor to the west compared to that east of the AST.

Table 2. Asymmetry of the Crestal Plateau From Bathymetric Profiles in Figure 6

		W Versus E "Young" Seafloor		"Young" Versus "Old" Seafloor		"Young" Terrain Limit[g]	
Profile[a]	Latitude[b]	H[c], m	H_{max},[d] m	H,[e] m	H_{max},[f] m	West, km	East, km
5	9°51.4′	−42.5	120.4	75.4	115.9	2.2	3.5
15b	9°49.7′	−11.5	54.4	50.7	53.0	2.0	2.1
15a	9°49.3′	−0.7	41.1	-	-	2.4	*>1.8*
3	9°48.4′	0.3	38.0	−55.9	−37.3	2.1	1.8
4	9°43.2′	−12.6	51.3	49.4	58.1	2.3	3.0
17	9°39.4′	9.0	38.6	39.9	43.7	3.2	3.0
7	9°36.9′	3.4	16.4	−55.0	−13.3	2.2	1.7
10	9°29.6′	−0.8	16.7	52.1	77.4	*>3.5*	1.0
12	9°27.2′	−3.9	16.3	−2.9	15.3	*>3.0*	1.4

[a] Camera Tow profile number, acquired during cruise AT11-7.
[b] Latitude of the AST crossing.
[c] Average seafloor difference between the East and the West flank within "young" seafloor (see area marked as a in Figure 6). Positive and negative values indicate a deeper on average E and W flank, respectively.
[d] Maximum difference in seafloor depth between the East and West flanks and within the "young" seafloor.
[e] Average seafloor difference between the "young" and the "old" seafloor at the same distance from the AST (see area marked as b in Figure 6). Positive values indicate that the "old" seafloor is deeper than the "young" seafloor on the conjugate side.
[f] Maximum difference in seafloor depth between the "old" and "young" bathymetric profiles at the same AST distance. Positive values indicate that the "old" seafloor is deeper than the "young" seafloor.
[g] Distance from the AST to the west and east limits of the "young" seafloor as identified in the sonar mosaics (Figure 2). Bold numbers indicate limits bound by faults. Profiles where the limit is beyond the profile are indicated in italics, and thus represent a minimum distance.

estimate that the difference in AST rim depth has been maintained over >∼1000 years (i.e., the minimum age difference between "young" and "old" seafloor), resulting in the deficit of ∼70 × 10^6 m^3/km of extrusive material on the east flank relative to the west flank (e.g., Figure 7c).

4. Discussion

[25] Combined high-resolution near-bottom bathymetry and side-scan sonar data along the axis of the EPR provide constraints on the initiation of faulting and fault evolution with time, as well as on their interaction with recently emplaced lava flows. This interaction results in the burial of fault scarps and fissures, and volcanic overprinting of a portion of the tectonic strain near-axis during volcanic events. Faults also play an important role in Layer 2A construction and evolution, by damming lava flows away from the AST, and helping to control the "young"/"old" seafloor boundary geometry.

4.1. Fault Nucleation and Evolution, and the Nature of the Active Deformation Zone

[26] The distribution of faults and fissures across the axis (Figures 2 and 4 and Table 1) suggests that deformation associated with the AST is decoupled from the development of normal faults developing further off-axis. The high fault and fissure density at the axis is caused by repeated dike intrusions associated with eruptions within and immediately proximal to the AST [*Chadwick and Embley*, 1998; *Fornari et al.*, 1998a, 2004; Soule et al., manuscript in preparation, 2007]. The traces of this deformation are efficiently covered by lava flows in the immediate vicinity of the AST, as seen in the sharp decrease in fissure and fault density within 500 m of the axis (Figure 4), and by the disappearance of sections of the AST (e.g., 9°52–9°54′N) under recent, undeformed flows (Soule et al., manuscript in preparation, 2007). Sections of the axis with a wide AST (>200 m wide, e.g., south of ∼9°36′N) probably reflect lower repaving rates in the recent past due to variations in magma supply over short time periods (∼1000 years) [e.g., *Fornari et al.*, 1998a; *Cormier et al.*, 2003].

[27] Faults appear to nucleate continuously in the immediate vicinity of the AST to the limit of our survey area (up to ∼5–6 km from the AST). This is suggested by the presence of small faults and fissures both on "young" and "old" seafloor, as well as by faults cross-cutting the "young"/"old" boundary at lava flow edges (e.g., off-axis flow in Figures 3b and 3d). Faults and fissures are efficiently buried near the AST, as shown by the large difference between "young" and "old" seafloor in fault density (e.g., 0.6 versus 2.8 km/km^2 for all faults), scarp height (e.g., 6 versus 11.5 m for inward facing faults), and estimated strain (e.g., 0.7 versus 2.9% for all faults, Table 1). This results

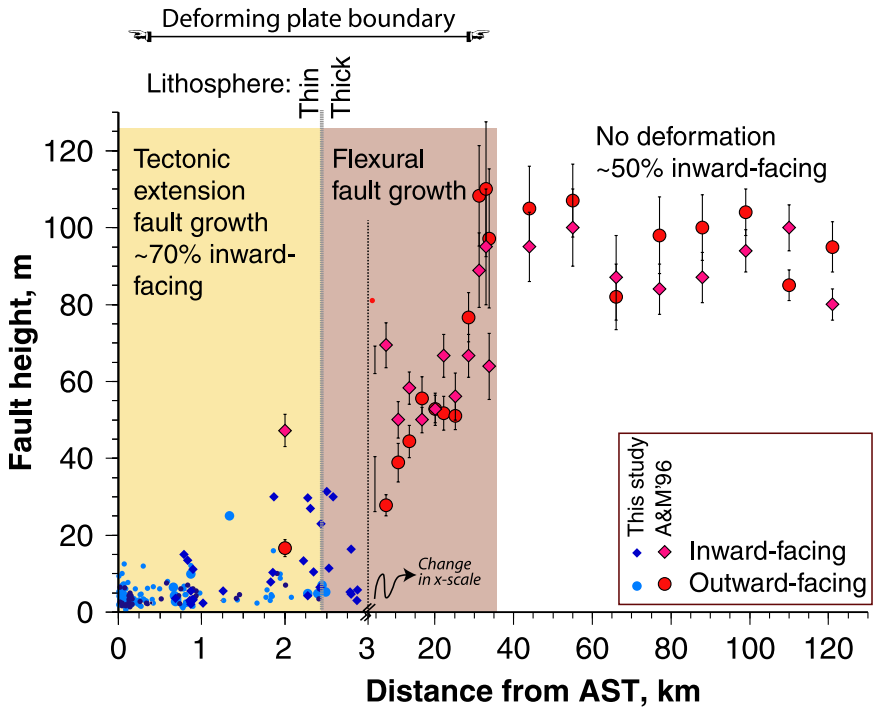

Figure 8. Variations in fault scarp height are shown with distance from the AST. A change in the horizontal scale is imposed at 3 km for clarity, as indicated. The deforming plate boundary has a width of ~40 km, over which inward and outward facing faults grow in size, and the proportion of inward facing faults decreases from ~70% at the axis to ~50% far from the axis. Data from this study are shown in light and dark blue, and those from *Alexander and Macdonald* [1996] (A&M'96) are shown in red and purple. See text for discussion.

in smooth "young" seafloor dominated by lava flows and volcanic features (e.g., flow fronts and mounds) lacking fault scarps. Small fault scarps in "old" seafloor are thus nucleated recently, and are preserved by the lack of volcanic repaving. The measured strain at the seafloor surface and in the immediate vicinity of the AST is therefore a minimum estimate, and is likely to be a small fraction (~20%) of the total tectonic strain.

[28] The deforming plate boundary in the study area shows two deformation zones, near- and off-axis, whose tectonic patterns and the origin of tectonic extension are distinct. About 70% of the faults within 5 km of the AST are inward facing, and accommodate ~80% of the tectonic strain. In contrast, previous studies have found that at distances >5 km off-axis 50% of the faults are inward facing and accommodate ~50% of the tectonic strain, while they continue to grow off axis to ~40 km [e.g., *Alexander and Macdonald*, 1996; *Crowder and Macdonald*, 2000]. Beyond this point both the characteristic fault scarp height (~100 m for both inward and outward facing faults) and the proportion of inward facing faults (~50%) is constant (Figure 8). A similar pattern of off-axis faulting is observed along the EPR at ~19°S [*Bohnenstiehl and Carbotte*, 2001], where 40% of the inward facing faults accommodate ~50% of the observed ~4% tectonic strain, and a narrow zone of active deformation extending ~8 km [*Bicknell et al.*, 1987] to ~15 km off axis [*Bohnenstiehl and Carbotte*, 2001].

[29] We propose that the transition in tectonic strain pattern is explained by the presence of a thin brittle lid above the AMC, and by the rapid increase in lithospheric thickness away from the axis (Figure 9). This area of the EPR is underlain at ~1.5–2 km depth by a continuous AMC whose width varies between ~250 m and >4 km [*Detrick et al.*, 1987; *Harding et al.*, 1993]. Seismic studies elsewhere along the EPR suggest that the base of a robust hydrothermal circulation system may be as close as ~50 m from the top of the AMC [*Singh et al.*, 1999], with a highly fractured, low velocity zone immediately above the melt lens [e.g., *Vera et al.*, 1990; *Singh et al.*, 1999]. The base of the brittle layer (~750°C) must thus lie between the AMC's roof and the base of the hydrothermal circulation

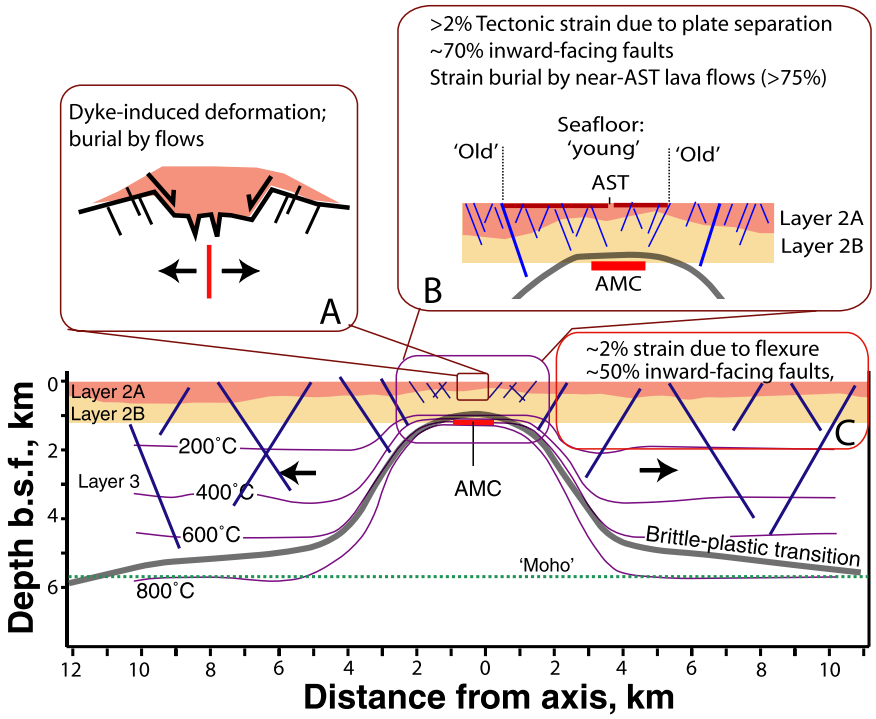

Figure 9. Cartoon showing different zones of fault formation and their interaction with near axis volcanism at the EPR. (a) Deformation in the immediate vicinity of the AST is associated with ground deformation triggered by dike intrusions, and rapid burial of tectonic structures by lava flows. (b) Over the AMC, deformation is dominated by inward facing faults (~70%) that accommodate a small part of the tectonic plate separation. Most of these faults (>75%) are either partially or totally buried by lava flows, as indicated by the difference in fault and fissure density between "old" and "young" seafloor at the same distance from the AST. Faults also limit the off-axis extent of recent lava flows by damming them. (c) Further off-axis faults continue to grow in height, and the proportion of outward facing faults increases to ~50%. This fault evolution is likely due to plate flexure [*Shah and Buck*, 2003] (Figure 8). Layer 2A growth may be partially controlled by tectonic subsidence and damming of flows, while the transition from the plate-extension to the plate-bending dominated sections of the young lithosphere near the ridge axis may correspond to the rapid increase in lithospheric thickness above the AMC [*Dunn et al.*, 2000; *Maclennan et al.*, 2005]. Layer 2A thickness is that at 9°30′N [*Harding et al.*, 1988], and the thermal structure is based on the seismic model of *Dunn et al.* [2000].

system, a narrow zone (<100 m) where the temperatures must descend abruptly from >1000°C to <500°C. The AMC is thus the base of a very thin (<2 km) brittle lid that is also the weakest part of the oceanic lithosphere.

[30] Isotherms are inferred to deepen rapidly off axis at the edge of the AMC due to efficient hydrothermal cooling [*Dunn et al.*, 2000; *Maclennan et al.*, 2005], increasing the brittle layer thickness to ~4 km or more over <1 km. Owing to the large contrast in thickness and therefore overall strength of the oceanic lithosphere, the small proportion of plate separation accommodated by faulting is likely to concentrate within the thin and narrow axial brittle lid, not within the thicker lithosphere off-axis. This deformation results in the observed ~70% of faults that face the AST and accommodate ~80% of the tectonic strain: a fault geometry that may be favored by the stress patterns in the vicinity of a shallow magma chamber [e.g., *Bohnenstiehl and Carbotte*, 2001]. Strain is likely to be preferentially localized at the transition from thin to thick brittle lithosphere, which is expected to occur at ~2–2.5 km from the axis at 9°30′N [*Dunn et al.*, 2000, Figure 10]. This distance is consistent with the occurrence of the largest fault scarps in our study area (>20 m, Figure 5).

[31] Deformation off-axis (>5 km) is likely to be associated with plate bending, instead of a tectonic component of plate separation. Thermal subsidence and rapid cooling can induce plate bending stresses [*Shah and Buck*, 2003]. These models predict deformation over a zone that varies between 15 km and 45 km in width, consistent with reported

widths of the plate boundary along the EPR [e.g., *Bicknell et al.*, 1987; *Edwards et al.*, 1991; *Alexander and Macdonald*, 1996; *Crowder and Macdonald*, 2000; *Bohnenstiehl and Carbotte*, 2001]. Models obtain strains of ~1–2% while assuming a fault angle of 60°; if a 45° angle is assumed instead it corresponds to strains of ~2–4% [e.g., *Bohnenstiehl and Carbotte*, 2001; *Carbotte and MacDonald*, 1994; this study]. Reported differences in fault facing direction between fast and slow spreading centers [*Carbotte and Macdonald*, 1990] may thus be due to different processes responsible for fault formation. The tectonic component of plate separation results in mostly inward facing faults (>60–70%), as observed at slow-spreading ridges, and in the near-axis area of the EPR. As plate bending results in ~50% inward facing faults and very low associated strains (1–2%), it may only be observable in fast spreading crust, where scarps formed near-axis are both small and often buried, and visible strains are low (~2% or less). This tectonic signature of bending may not be visible at slow-spreading crust, owing to the higher strains (~10% or more) and the large size of scarps (>100 m) generated at the axis [e.g., *Cowie et al.*, 1993; *Carbotte and MacDonald*, 1994; *Shaw and Lin*, 1993; *Escartín et al.*, 1999].

4.2. Tectonic Strain Estimates

[32] Tectonic strain estimates from seafloor faulting studies are biased by both volcanic processes and assumptions regarding fault geometry. The observable tectonic strain in our study area is very small within "young" seafloor (<1%), and increases to >2% in "old" seafloor, lower than estimates for other EPR areas which range from ~4% (EPR, 19°S [e.g., *Bohnenstiehl and Carbotte*, 2001]) to ~5–10% (EPR 11°–15°N [*Cowie et al.*, 1993]) up to 18% (Explorer Ridge [*Deschamps et al.*, 2007]). Due to the continuous volcanic emplacement and efficient seafloor resurfacing at fast spreading ridges that result in the burial of fault scarps, strain estimates derived from this and other studies are likely to underestimate the real tectonic strain. Most studies of strain and faulting assume a ~45° fault dip [e.g., *Cowie et al.*, 1993; *Carbotte and MacDonald*, 1994; *Bohnenstiehl and Carbotte*, 2001], consistent with earthquake focal mechanisms [e.g., *Thatcher and Hill*, 1995] allowing for a direct comparison of results among different study areas. Steeper faults would result in significantly lower absolute strains (i.e., 40% lower for a 60° fault dip). Our results suggest that, at the same distance of the AST, as much as ~80% of the tectonic strain may be buried by young lava flows (Figure 4b). The real tectonic strain within "young" seafloor may thus be >2%, instead of the estimated ~0.5% surface strain observed near-axis, and would increase to >4% in "old" seafloor instead of the >2% estimate (see Table 1). Accurate estimates of the buried and observable surface strain require precise knowledge on the width of the active deformation zone, the distribution of strain throughout this area, the recurrence time and size of eruptions, and the precise fault geometry at depth. While we could gain insights into some of these parameters with high-resolution, near-bottom multibeam systems, many of these cannot be constrained at the present time (i.e., depth geometry of faults, statistically determined recurrence and volume of lava flows erupting from the AST).

4.3. Effects of Faulting on Lava Flow Length and the Construction of Layer 2A

[33] The Layer 2A thickening from ~200 m to ~500 m over 1–2 km from the axis [e.g., *Harding et al.*, 1993; *Vera and Diebold*, 1994], which occurs within the thin brittle lid overlying the AMC, requires both short (~100 m) and long flows (~1500 m) [*Hooft et al.*, 1996; *Schouten et al.*, 1999]. On the basis of our observations, the length of these flows is partially controlled by faulting (Figure 2). The population of short lava flows represent small volume eruptions from the AST that are well-documented in the side-scan data [*Fornari et al.*, 2004; Soule et al., manuscript in preparation, 2007]. *Hooft et al.* [1996] proposed flow lengths of ~1500 m which is similar to the ~1–2 km distance from the AST to our observed boundary between "young" and "old" seafloor. At that distance, the increasing rate at which inward facing fault scarps are formed and grow, and the decreasing frequency of emplacement of long lava flows capable of reaching those scarps results in an efficient damming of lava flows. This distance is also comparable to the extent of the central anomaly magnetic high in this area [e.g., *Schouten et al.*, 1999, 2002; C. M. Williams et al., The central anomaly magnetization high documents variations in crustal accretionary processes along the East Pacific Rise (9°55–25′N), submitted to *Geochemistry, Geophysics, Geosystems*, 2007], and therefore within the zone of most recent volcanic emplacement. A similar pattern of faulting and Layer 2A growth can be inferred for the EPR at 17°10′–40′S, where Layer 2A acquires its full thickness ~5 km from the axis. At that location

faulting and volcanism interact beyond ~5 km and bending-related faults cut and modify the structure of the extrusive pile beyond ~5 km, with no volcanic interaction [see *Carbotte et al.*, 1997, Figure 9].

[34] In addition to damming lava flows, faulting promotes subsidence of the volcanic pile, facilitating the emplacement of additional of material needed for Layer 2A growth. However, the extent of tectonic deformation and associated subsidence in the near-AST region is difficult to identify as it is efficiently overprinted by lava flows. The population of shorter lava flows systematically buries the faults accommodating plate separation and the component of vertical subsidence associated with them. In areas where volcanic deposition is asymmetric (e.g., 9°28′N), we have found that faulting can produce subsidence of >100 m within 3–4 km from the axis (Figures 6 and 7), corresponding to the difference in depth between conjugate flanks, or to the development of off-axis graben. The graben can also trap large amounts of volcanic material until they are fully infilled, as suggested by the some of the bathymetric profiles (see arrows in Figure 6). Tectonic subsidence can amount to ~100–200 m if we assume a total tectonic strain of 5–10% accommodated by 45° faults over a 4-km wide zone centered about the AST. This value increases to ~170 to 350 m for 60° faults. With Layer 2A thickening at the EPR ~300 m within ~2 km of the axis [e.g., *Christeson et al.*, 1994; *Harding et al.*, 1993; *Vera and Diebold*, 1994], faulting can account for >30% to 100% of the total subsidence required for its formation.

[35] Areas characterized by an asymmetry in seafloor topography can be interpreted to indicate a deficit in volcanic emplacement on the deeper flank, assuming that subsidence is symmetric. In the 9°29′N area (Figure 7), the E flank shows a deficit of $\sim 70 \times 10^6$ m^3 per km of ridge axis (see section 3.3) relative to the W flank. Assuming a typical eruption volume at the EPR of $\sim 3–5 \times 10^6$ m^3 based on field observations [*Gregg et al.*, 1996; *Perfit and Chadwick*, 1998; *Soule et al.*, 2006], this deficit can correspond to ~15–25 eruptions per unit length of ridge. Estimates of eruption recurrence interval from numerical models range between 15–70 years [e.g., *Hooft et al.*, 1996; *Bowles et al.*, 2006]; the lower end of this range is consistent with the 10–15 years periodicity proposed by various investigators [e.g., *Haymon*, 1996; *Gregg et al.*, 1996; *Perfit and Chadwick*, 1998]. The ridge-crest asymmetry we have identified at 9°29′N and other areas (see profiles in Figure 6) can thus correspond to a lack of volcanic deposition on one flank of the ridge that could be for periods of ~500 years to several thousands of years.

5. Conclusions

[36] Analysis of fault data from high-resolution side-scan sonar and bathymetry data along a ~4 km to 8 km wide area centered along the EPR AST between 9°25′N and 9°58′N demonstrates that interaction between volcanic and tectonic processes influences the construction of the oceanic extrusive layer at a fast spreading MOR. We identify two volcanic provinces at the EPR crest between 9°25′N and 9°58′N on the basis of their acoustic backscatter: (1) high reflectivity "young," recently repaved seafloor, and (2) low reflectivity "old" sediment covered seafloor. The boundary between these provinces is distinct and most commonly reflects the damming of lava flows by inward facing fault scarps, and in a few locations, the limit of individual lava flows emplaced over sedimented seafloor.

[37] Comparison of fault parameters demonstrates that at the same distance from the AST the density of faulting and estimated tectonic strain on "old" seafloor are 4–5 times higher than those on "young" repaved seafloor. These data demonstrate that volcanism efficiently buries, either partially or totally, faults nucleating and developing within 2 km of the AST. Sufficiently high fault scarps act as topographic barriers and are a key factor determining the typical length of long lava flows (1–2 km) required to accurately model the development and geometry of Layer 2A. These topographic barriers correlate well with the extent of the central anomaly magnetic high, a marker of recent volcanic emplacement. Faults also provide a mechanism for the tectonic subsidence of lava flows that can account from 30% to 100% of the ~300 m thickening of Layer 2A between the axis and ~2 km off-axis, where it is fully developed.

[38] The morphology of the AST can locally control the preferential volcanic deposition on one flank of the EPR crestal plateau. This asymmetry is present at several sites within the study area, and appears to be sustained over periods >~1000 years. Asymmetric deposition results in ridge-crest volume surpluses or deficits that locally can reach $>70 \times 10^6$ m^3 per km of ridge axis, and corresponds to a cumulative volume of ~15–25 "typical" EPR

volcanic eruptions, based on available estimates of eruption sizes.

[39] We observe that at least 2% of the plate separation in the study area is accommodated by tectonic extension, primarily along inward facing faults that comprise ~70% of the fault population. Tectonism occurs dominantly within a narrow zone extending ~2 km from the AST, corresponding to the thin brittle layer overlying the AMC. Due to the efficient burial of fault scarps by near-AST lava flows, the actual amount of plate separation accommodated by tectonic strain may be significantly higher than that inferred from fault observations.

[40] Fault scarps most effectively block lava flows at distances of 1–2 km from the AST. At this distance fault growth appears to outpace the frequency of volcanic deposition, allowing the development of scarps that are higher than the typical lava flow thickness. Fault growth in this area is associated with the abrupt increase in lithospheric thickness at the edges of the AMC, as suggested by seismic data. Faulting at distances >2 km from the AST appears to be controlled by lithospheric bending due to cooling, and not by the accommodation of the tectonic component of plate separation. Faults off-axis show patterns that differ from those near-axis (<2 km), with an equal proportion of inward and outward facing faults accommodating ~4% tectonic strain, consistent with numerical model predictions of plate bending.

Acknowledgments

[41] We thank the captain, officers, crew, and science party of R/V *Atlantis* during cruises AT7-4 and AT11-7 and the WHOI National Deep Submergence Facility shipboard and shore-based operations groups for their assistance and diligence in collecting these data. V. Ferrini processed all Alvin bathymetry collected during AT11-7 and used in this paper. Discussions with J. Maclennan, S. Singh, M. Cannat, D. K. Smith, and J. Cann are gratefully acknowledged and contributed to this research. In-depth comments by R. C. Searle, R. Soliva, and the Associate Editor M. R. Reid greatly helped us to improve this manuscript. The field and laboratory studies were supported by NSF grants OCE-9819261 (to H.S., M.A.T., and D.J.F.), OCE-0525863 (D.J.F. and S.A.S.), OCE-0138088 (M.P.), WHOI Vetlesen Foundation Funds (J.E., D.J.F., and S.A.S.). Additional support by INSU/CNRS to J.E. is also acknowledged. This is IPGP contribution 2205.

References

Alexander, R. T., and K. C. Macdonald (1996), SeaBeam, SeaMARC II and *Alvin*-based studies of faulting on the East Pacific Rise 9°20′N–9°50′N, *Mar. Geophys. Res.*, *18*, 557–587.

Bicknell, J. D., J.-C. Sempere, K. C. Macdonald, and P. J. Fox (1987), Tectonics of a fast-spreading center: A deep-tow and SeaBeam survey on the East Pacific Rise at 19°30′S, *Mar. Geophys. Res.*, *9*, 25–45.

Bohnenstiehl, D. R., and S. M. Carbotte (2001), Faulting patterns near 19°30′S on the East Pacific Rise: Fault formation and growth at a superfast spreading center, *Geochem. Geophys. Geosyst.*, *2*(9), doi:10.1029/2001GC000156.

Bowles, J., J. S. Gee, D. V. Kent, M. R. Perfit, S. A. Soule, and D. J. Fornari (2006), Paleointensity applications to timing and extent of eruptive activity, 9°–10°N East Pacific Rise, *Geochem. Geophys. Geosyst.*, *7*, Q06006, doi:10.1029/2005GC001141.

Carbotte, S., and K. MacDonald (1992), East Pacific Rise 8°–10°30′N: Evolution of ridge segments and discontinuities from SeaMARC II and three dimensional magnetic studies, *J. Geophys. Res.*, *97*, 6959–6982.

Carbotte, S., and K. C. MacDonald (1994), Comparison of tectonic fabric at intermediate, fast, and super fast spreading ridges: Influence of spreading rate, plate motions, and ridge segmentation on fault patterns, *J. Geophys. Res.*, *99*, 13,609–13,631.

Carbotte, S. M., J. C. Mutter, and L. Xu (1997), Contribution of volcanism and tectonism to axial and flank morphology of the southern East Pacific Rise, 17°10′–17°40′S, from a study of layer 2A geometry, *J. Geophys. Res.*, *102*, 10,165–10,184.

Carbotte, S. M., W. B. F. Ryan, W. Jin, M. Cormier, E. Bergmanis, J. Sinton, and S. White (2003), Magmatic subsidence of the East Pacific Rise (EPR) at 18°14′S revealed through fault restoration of ridge crest bathymetry, *Geochem. Geophys. Geosyst.*, *4*(1), 1008, doi:10.1029/2002GC000337.

Chadwick, W. W., and R. W. Embley (1998), Graben formation associated with recent dike intrusions and volcanic eruptions on the mid-ocean ridge, *J. Geophys. Res.*, *103*, 9807–9825.

Chadwick, W. W.Jr., D. S. Scheirer, R. W. Embley, and H. P. Johnson (2001), High-resolution bathymetric surveys using scanning sonars: Lava flow morphology, hydrothermal vents and geologic structure at recent eruption sites on the Juan de Fuca Ridge, *J. Geophys. Res.*, *106*, 16,075–16,100.

Christeson, G. L., G. M. Purdy, and G. J. Fryer (1992), Structure of young upper crust at the East Pacific Rise near 9°30′N, *Geophys. Res. Lett.*, *19*, 1045–1048.

Christeson, G. L., G. M. Purdy, and G. J. Fryer (1994), Seismic constraints on shallow crustal emplacement processes at the fast spreading East Pacific Rise, *J. Geophys. Res.*, *99*, 17,957–17,973.

Christeson, G. L., G. M. Kent, G. M. Purdy, and R. S. Detrick (1996), Extrusive thickness variability at the East Pacific Rise, 9°–10°N: Constraints from seismic techniques, *J. Geophys. Res.*, *101*, 2859–2873.

Christeson, G. L., P. R. Shaw, and J. D. Garmany (1997), Shear and compressional wave structure of the East Pacific Rise, 9°–10°N, *J. Geophys. Res.*, *102*, 7821–7835.

Cochran, J. R., D. J. Fornari, B. J. Coakley, R. Herr, and M. A. Tivey (1999), Continuous near-bottom gravity measurements made with a BGM-3 gravimeter in DSV *Alvin* on the East Pacific Rise crest near 9°31′ and 9°50′N, *J. Geophys. Res.*, *104*, 10,841–10,861.

Collier, J., and S. C. Singh (1997), Detailed structure of the top of the melt body beneath the East Pacific Rise at 9°40′N from waveform inversion of seismic reflection data, *J. Geophys. Res.*, *102*, 20,287–20,304.

Cormier, M.-H., W. B. F. Ryan, A. K. Shah, W. Jin, A. M. Bradley, and D. R. Yoerger (2003), Waxing and waning volcanism along the East Pacific Rise on a millennium time scale, *Geology*, *31*, 633–636.

Cowen, J. P., et al. (2007), Volcanic eruption at the East Pacific Rise near 9°50′N, *Eos Trans. AGU*, in press.

Cowie, P. A., C. H. Scholz, M. Edwards, and A. Malinverno (1993), Fault strain and seismic coupling on mid-ocean ridges, *J. Geophys. Res.*, *98*, 17,911–17,920.

Cowie, P. A., A. Malinverno, W. B. F. Ryan, and M. H. Edwards (1994), Quantitative fault studies on the East Pacific Rise: A comparison of sonar imaging techniques, *J. Geophys. Res.*, *99*, 15,205–15,218.

Crowder, L. K., and K. C. Macdonald (2000), New constraints on the width of the zone of active faulting on the East Pacific Rise 8°30′N–10°00′N from SeaBeam bathymetry and SeaMARC II side-scan sonar, *Mar. Geophys. Res.*, *21*, 513–527.

Dawers, N. H., M. H. Anders, and C. H. Scholz (1993), Growth of normal faults: Displacement-length scaling, *Geology*, *21*, 1107–1110.

Deschamps, A., M. Tivey, R. W. Embley, and W. W. Chadwick (2007), Quantitative study of the deformation at Southern Explorer Ridge using high-resolution bathymetric data, *Earth Planet. Sci. Lett.*, doi:10.1016/j.epsl.2007.04.007, in press.

Detrick, R. S., P. Buhl, E. Vera, J. Mutter, J. Orcutt, J. Madsen, and T. Brocher (1987), Multichannel seismic imaging of a crustal magma chamber along the East Pacific Rise between 9°N and 13°N, *Nature*, *326*, 35–41.

Dunn, A., D. R. Toomey, and S. C. Solomon (2000), Three-dimensional seismic structure and physical properties of the crust and shallow mantle beneath the East Pacific Rise at 9°30′N, *J. Geophys. Res.*, *105*, 23,537–23,555.

Edwards, M. H., D. J. Fornari, A. Malinverno, W. B. F. Ryan, and J. Madsen (1991), The regional tectonic fabric of the East Pacific Rise from 12°50′ to 15°10′N, *J. Geophys. Res.*, *96*, 7995–8017.

Engels, J. L., M. H. Edwards, D. J. Fornari, M. R. Perfit, and J. R. Cann (2003), A new model for submarine volcanic collapse formation, *Geochem. Geophys. Geosyst.*, *4*(9), 1077, doi:10.1029/2002GC000483.

Escartín, J., P. A. Cowie, R. C. Searle, S. Allerton, N. C. Mitchell, C. J. MacLeod, and A. P. Slootweg (1999), Quantifying tectonic strain and magmatic accretion at a slow spreading ridge segment, Mid-Atlantic Ridge, 29°N, *J. Geophys. Res.*, *104*, 10,421–10,437.

Ferrini, V. L., D. J. Fornari, T. M. Shank, J. C. Kinsey, M. A. Tivey, S. A. Soule, S. M. Carbotte, L. L. Whitcomb, D. Yoerger, and J. Howland (2007), Submeter bathymetric mapping of volcanic and hydrothermal features on the East Pacific Rise crest at 9°50′N, *Geochem. Geophys. Geosyst.*, *8*, Q01006, doi:10.1029/2006GC001333.

Fornari, D. J. (2003), A new deep-sea towed digital camera and multi-rock coring system, *Eos Trans. AGU*, *84*, 69, 73.

Fornari, D. J., R. M. Haymon, M. R. Perfit, T. K. P. Gregg, and M. H. Edwards (1998a), Geological characteristics and evolution of the axial zone on fast spreading mid-ocean ridges: Formation of an axial summit trough along the East Pacific Rise, 9°–10°N, *J. Geophys. Res.*, *103*, 9827–9855.

Fornari, D. J., T. Shank, K. L. Von Damm, T. K. P. Gregg, M. Lilley, G. Levai, A. Bray, R. M. Haymon, M. R. Perfit, and R. Lutz (1998b), Time-series temperature measurements at high-temperature hydrothermal vents, East Pacific Rise 9°49′–51′N: Monitoring a crustal cracking event, *Earth Planet. Sci. Lett.*, *160*, 419–431.

Fornari, D. J., et al. (2004), Submarine lava flow emplacement at the East Pacific Rise 9°50′N: Implications for uppermost ocean crust stratigraphy and hydrothermal fluid circulation, in *Mid-ocean Ridges: Hydrothermal Interactions Between the Lithosphere and Oceans*, *Geophys. Monogr. Ser.*, vol. 148, edited by C. R. German, J. Lin, and L. M. Parson, pp. 187–218, AGU, Washington, D. C.

Garry, W. B., T. K. P. Gregg, S. A. Soule, and D. J. Fornari (2006), Formation of submarine lava channel textures: Insights from laboratory simulations, *J. Geophys. Res.*, *111*, B03104, doi:10.1029/2005JB003796.

Goldstein, S. J., M. T. Murrlell, and R. W. Williams (1993), ^{231}Pa and ^{230}Th chronology of mid-ocean ridge basalts, *Earth Planet. Sci. Lett.*, *115*, 151–160.

Gregg, T. K. P., J. Fornari, M. R. Perfit, R. M. Haymon, and J. H. Fink (1996), Rapid emplacement of a mid-ocean ridge lava flow on the East Pacific Rise at 9°46′–51′N, *Earth Planet. Sci. Lett.*, *144*, 1–7.

Harding, A. J., G. M. Kent, and J. A. Orcutt (1993), A multichannel seismic investigation of upper crustal structure at 9°N on the East Pacific Rise: Implications for crustal accretion, *J. Geophys. Res.*, *98*, 13,925–13,944.

Haymon, R. M. (1996), The response of ridge crest hydrothermal systems to segmented, episodic magma supply, in *Tectonic, Magmatic, Hydrothermal, and Biological Segmentation of Mid-Ocean Ridges*, edited by C. J. MacLeod, P. Tyler, and C. L. Walker, *Geol. Soc. Spec. Publ.*, *118*, 157–168.

Haymon, R. M., D. J. Fornari, M. H. Edwards, S. Carbotte, D. Wright, and K. C. Macdonald (1991), Hydrothermal vent distribution along the East Pacific Rise crest (9°09′–54′N) and its relationship to magmatic and tectonic processes on fast-spreading mid-ocean ridges, *Earth Planet. Sci. Lett.*, *104*, 513–534.

Haymon, R. M., et al. (1993), Volcanic eruption of the mid-ocean ridge along the East Pacific Rise crest at 9°45–52′N: Direct submersible observations of seafloor phenomena associated with an eruption event in April, 1991, *Earth Planet. Sci. Lett.*, *119*, 85–101.

Hey, R., et al. (2004), Tectonic/volcanic segmentation and controls on hydrothermal venting along Earth's fastest seafloor spreading system, EPR 27°–32°S, *Geochem. Geophys. Geosyst.*, *5*, Q12007, doi:10.1029/2004GC000764.

Hooft, E. E. E., H. Schouten, and R. S. Detrick (1996), Constraining crustal emplacement processes from the variation in layer 2A thickness at the East Pacific Rise, *Earth Planet. Sci. Lett.*, *142*, 289–309.

Kent, G. M., A. J. Harding, and J. A. Orcutt (1993), Distribution of magma beneath the East Pacific Rise between the Clipperton Transform and the 9°17′N deval from forward modeling of common depth point data, *J. Geophys. Res.*, *98*, 13,945–13,969.

Kinsey, J. C., and L. L. Whitcomb (2002), Towards in-situ calibration of gyro and Doppler navigation sensors for precision underwater vehicle navigation, in *Proceedings. ICRA '02: IEEE International Conference on Robotics and Automation, 2002*, vol. 4, edited by J. C. Kinsey and L. L. Whitcomb, pp. 4016–4023, Inst. of Electr. and Electron. Eng., New York.

Kinsey, J. C., and L. L. Whitcomb (2004), Preliminary field experience with the DVLNAV integrated navigation system for oceanographic submersibles, *Control Eng. Pract.*, *12*, 1541–1549.

Kurras, G. J., D. J. R. Fornari, M. H. Edwards, M. R. Perfit, and M. C. Smith (2000), Volcanic morphology of the East Pacific Rise Crest 9°49′–52′: Implications for volcanic emplacement processes at fast-spreading mid-ocean ridges, *Mar. Geophys. Res.*, *21*, 23–41.

Lee, S.-M., and S. C. Solomon (1995), Constraints from Sea-Beam bathymetry on the development of normal faults on the East Pacific Rise, *Geophys. Res. Lett.*, *22*, 3135–3138.

Macdonald, K. C., et al. (1992), The East Pacific Rise and its flanks 8–18°N: History of segmentation, propagation and spreading direction based on SeaMARC and Sea Beam studies, *Mar. Geophys. Res.*, *14*, 299–344.

Macdonald, K. C., P. J. Fox, R. T. Alexander, R. Pockalny, and P. Gente (1996), Volcanic growth faults and the origin of Pacific abyssal hills, *Nature*, *380*, 125–129.

Maclennan, J., T. Hulme, and S. C. Singh (2005), Cooling of the lower oceanic crust, *Geology*, *33*, 357–360.

Mitchell, N. C. (1993), A model for attenuation of backscatter due to sediment accumulation and its implication to determine sediment thickness with GLORIA sidescan sonar, *J. Geophys. Res.*, *98*, 22,477–22,493.

Perfit, M. R., and W. W. Chadwick (1998), Magmatism at mid-ocean ridges: Constraints from volcanological and geochemical investigations, in *Faulting and Magmatism at Mid-ocean Ridges*, *Geophys. Monogr. Ser.*, vol. 106, edited by W. R. Buck et al., pp. 59–115, AGU, Washington, D. C.

Perfit, M. R., D. J. Fornari, M. C. Smith, J. F. Bender, C. H. Langmuir, R. M. Haymon, and J. F. Bender (1994), Small scale spatial and temporal variations in mid-ocean ridge crest magmatic processes, *Geology*, *22*, 375–379.

Scheirer, D. S., D. J. Fornari, S. E. Humphris, and S. Lerner (2000), High-resolution seafloor mapping using the DSL-120 sonar system: Quantitative assessment of sidescan and phase-bathymetry data from the Lucky Strike segment of the Mid-Atlantic Ridge, *Mar. Geophys. Res.*, *21*, 121–142.

Schouten, H., M. A. Tivey, D. J. Fornari, and J. R. Cochran (1999), Central anomaly magnetization high: Constraints on the volcanic construction and architecture of seismic layer 2A at a fast-spreading mid-ocean ridge, the EPR at 9°30′–50′N, *Earth Planet. Sci. Lett.*, *169*, 37–50.

Schouten, H., M. Tivey, D. Fornari, D. Yoerger, A. Bradley, P. Johnson, M. Edwards, and T. Kurokawa (2002), Lava transport and accumulation processes on EPR 9°27′ to 10°N: Interpretations based on recent near-bottom sonar imaging and seafloor observations using ABE, *Alvin* and a new digital deep sea camera, *Eos Trans. AGU*, *83*(47), Fall Meet. Suppl., Abstract T11C-1262.

Searle, R. C. (1984), GLORIA survey of the East Pacific Rise near 3.5°S: Tectonic and volcanic characteristics of a fast-spreading mid-ocean rise, *Tectonophysics*, *101*, 319–344.

Searle, R. C., and A. S. Laughton (1977), Sonar studies of the Mid-Atlantic Ridge and Kurchatov Fracture Zone, *J. Geophys. Res.*, *82*, 5313–5328.

Shah, A., and W. R. Buck (2003), Plate bending stresses at axial highs, and implications for faulting behavior, *Earth Planet. Sci. Lett.*, *211*, 343–356.

Shaw, P. R., and J. Lin (1993), Causes and consequences of variations in faulting style at the Mid-Atlantic Ridge, *J. Geophys. Res.*, *98*, 21,839–21,851.

Sims, K. W. W., et al. (2003), Aberrant youth: Chemical and isotopic constraints on the origin of off-axis lavas from the East Pacific Rise, 9°–10°N, *Geochem. Geophys. Geosyst.*, *4*(10), 8621, doi:10.1029/2002GC000443.

Singh, H., L. L. Whitcomb, D. Yoerger, and O. Pizarro (2000), Micro bathymetric mapping from underwater vehicles in the deep ocean, *J. Comput. Vision Image Understanding*, *79*, 143–161.

Singh, S. C., J. S. Collier, A. J. Harding, G. M. Kent, and J. A. Orcutt (1999), Seismic evidence for a hydrothermal layer above the solid roof of the axial magma chamber at the southern East Pacific Rise, *Geology*, *27*, 219–222.

Sohn, R. A., and K. W. W. Sims (2005), Bending as a mechanism for triggering off-axis volcanism on the East Pacific Rise, *Geology*, *33*, 93–96.

Soliva, R., A. Benedicto, and L. Maerten (2006), Spacing and linkage of confined normal faults: Importance of mechanical thickness, *J. Geophys. Res.*, *111*, B01402, doi:10.1029/2004JB003507.

Soule, S. A., D. J. Fornari, M. R. Perfit, M. A. Tivey, W. I. Ridley, and H. Schouten (2005), Channelized lava flows at the East Pacific Rise crest 9°–10°N: The importance of off-axis lava transport in developing the architecture of young oceanic crust, *Geochem. Geophys. Geosyst.*, *6*, Q08005, doi:10.1029/2005GC000912.

Soule, S., et al. (2006), Extent and dynamics of the 2005–06 volcanic eruptions of the East Pacific Rise, 9°46′–56′N, *Eos Trans. AGU*, *87*(52), Fall Meet. Suppl., Abstract V13C-04.

Stewart, W. K., D. Chu, S. Malik, S. Lerner, and H. Singh (1994), Quantitative seafloor characterization using a bathymetric sidescan sonar, *IEEE J. Oceanic Eng.*, *19*, 599–610.

Thatcher, W., and D. P. Hill (1995), A simple model for the fault-generated morphology of slow-spreading mid-ocean ridges, *J. Geophys. Res.*, *100*, 561–570.

Tolstoy, M., et al. (2006), A sea-floor spreading event captured by seismometers, *Science*, *314*, 1920–1922.

Toomey, D. R., G. M. Purdy, S. C. Solomon, and W. S. D. Wilcock (1990), The three-dimensional seismic velocity structure of the East Pacific Rise near latitude 9°30′N, *Nature*, *347*, 639–645.

Toomey, D. R., S. C. Solomon, and G. M. Purdy (1994), Tomographic imaging of the shallow crustal structure of the East Pacific Rise at 9°30′, *J. Geophys. Res.*, *99*, 24,135–24,157.

Vera, E. E., and J. B. Diebold (1994), Seismic imaging of oceanic layer 2A between 9°30′ and 10°N on the East Pacific Rise from two-ship wide-aperture profiles, *J. Geophys. Res.*, *99*, 3031–3041.

Vera, E. E., C. J. Mutter, P. Buhl, J. A. Orcutt, A. J. Harding, M. E. Kappus, R. S. Detrick, and T. M. Brocher (1990), The structure from 0- to 0. 2-m.y.-old oceanic crust at 9°N on the East Pacific Rise from expanded spread profiles, *J. Geophys. Res.*, *95*, 15,529–15,556.

White, S. M., K. C. Macdonald, and R. M. Haymon (2000), Basaltic lava domes, lava lakes, and volcanic segmentation on the southern East Pacific Rise, *J. Geophys. Res.*, *105*, 23,519–23,536.

White, S. M., K. C. Macdonald, and J. M. Sinton (2002), Volcanic mound fields on the East Pacific Rise, 16°–19°S: Low effusion rate at overlapping spreading centers for the past 1 Myr, *J. Geophys. Res.*, *107*(B10), 2240, doi:10.1029/2001JB000483.

Wright, D. J., R. M. Haymon, and D. J. Fornari (1995a), Crustal fissuring and its relationship to magmatic and hydrothermal processes on the East Pacific Rise crest (9°12′ to 54°N), *J. Geophys. Res.*, *100*, 6097–6120.

Wright, D. J., R. M. Haymon, and K. C. MacDonald (1995b), Breaking new ground: Estimates of crack depth along the axial zone of the East Pacific Rise (9°12′–54′N), *Earth Planet. Sci. Lett.*, *134*, 441–457.

Yoerger, D. R., A. M. Bradley, B. B. Walden, H. Singh, and R. Bachmayer (1998), Surveying a subsea lava flow using the Autonomous Benthic Explorer (ABE), *Int. J. Syst. Sci.*, *10*, 1031–1044.